MATERIALS SCIENCE

A chiral switchable photovoltaic ferroelectric 1D perovskite

Yang Hu^{1*}, Fred Florio^{1,2*}, Zhizhong Chen¹, W. Adam Phelan³, Maxime A. Siegler³, Zhe Zhou¹, Yuwei Guo¹, Ryan Hawks¹, Jie Jiang^{1,4}, Jing Feng⁴, Lifu Zhang¹, Baiwei Wang¹, Yiping Wang¹, Daniel Gall¹, Edmund F. Palermo¹, Zonghuan Lu², Xin Sun², Toh-Ming Lu², Hua Zhou⁵, Yang Ren⁵, Esther Wertz^{2†}, Ravishankar Sundararaman^{1,2†}, Jian Shi^{1,6†}

Spin and valley degrees of freedom in materials without inversion symmetry promise previously unknown device functionalities, such as spin-valleytronics. Control of material symmetry with electric fields (ferroelectricity), while breaking additional symmetries, including mirror symmetry, could yield phenomena where chirality, spin, valley, and crystal potential are strongly coupled. Here we report the synthesis of a halide perovskite semiconductor that is simultaneously photoferroelectricity switchable and chiral. Spectroscopic and structural analysis, and first-principles calculations, determine the material to be a previously unknown low-dimensional hybrid perovskite (R)-(-)-1-cyclohexylethylammonium/(S)-(+)-1 cyclohexylethylammonium) Pbl₃. Optical and electrical measurements characterize its semiconducting, ferroelectric, switchable pyroelectricity and switchable photoferroelectric properties. Temperature dependent structural, dielectric and transport measurements reveal a ferroelectric-paraelectric phase transition. Circular dichroism spectroscopy confirms its chirality. The development of a material with such a combination of these properties will facilitate the exploration of phenomena such as electric field and chiral enantiomer–dependent Rashba-Dresselhaus splitting and circular photogalvanic effects.

Copyright © 2020
The Authors, some rights reserved; exclusive licensee American Association for the Advancement of Science. No claim to original U.S. Government Works. Distributed under a Creative Commons Attribution NonCommercial License 4.0 (CC BY-NC).

INTRODUCTION

Recently, ferroelectric semiconductors with strong spin-orbit coupling emerged as theoretically promising candidates for previously unavailable electronic functionalities such as spin-orbitronics, by exploiting the electric field–switchable Rashba-Dresselhaus effect (1-6). The ability to break inversion symmetry in a field-dependent manner is the primary source of this phenomenon. Breaking additional symmetries, such as chirality, in spin-orbit ferroelectric semiconductors would introduce additional perturbations in the Rashba-Dresselhaus physics that could lead to further fine-grained control of the coupled optical, spin, valley, and electronic properties of these materials [e.g., chirality-controlled circular photogalvanic effect (7,8)].

Bringing together spin-orbit-split ferroelectricity and chirality necessitates overcoming two challenges. First, most ferroelectric materials with strong spin-orbit coupling (2–6) have too low of a bandgap for unambiguously achieving ferroelectricity in experiment, resulting in a long-standing debate about whether these materials are even ferroelectric. Second, common chiral materials (9) that exhibit spin-selectivity to photons (10, 11) and electrons (12, 13), such as sodium ammonium tartrate, (S)-alanine, and cholesteric liquid crystals, typically have large bandgaps with response only in the ultraviolet (UV) and poor carrier mobilities. Here, we theoretically design and experimentally realize an electrically switchable, chiral,

spin-orbit ferroelectric material in a hybrid lead halide perovskite semiconductor.

Organic-inorganic halide perovskites (14-17) have shown great potential in photovoltaic and electro-optical devices due to their excellent semiconducting properties. The lead iodine octahedra in hybrid perovskites control the band-edge electronic structure and make them good semiconductors with strong spin-orbit coupling, while the organic groups serve as structural and chemical stabilizers. The organic groups provide the flexibility to explore unique functionalities, such as the ferroelectricity and chirality explored here (Fig. 1), while retaining the desirable semiconducting behavior. Taking such design approach, notable seminar works (18-24) in this field on hybrid perovskite have been inspiring the search of unprecedented materials performance and previously unknown properties. Recently, Xiong et al. (18) reported the two-dimensional (2D) ferroelectric perovskite in the form of chiral enantiomers. Here, specifically, by using chiral (R)-(-)-1-cyclohexylethylamine (R-CYHEA, C₈H₁₅NH₂) or (S)-(+)-1-cyclohexylethylamine (S-CYHEA, C₈H₁₅NH₂) for the organic group, we have successfully designed and synthesized a pair of enantiomers R-CYHEAPbI3 and S-CYHEAPbI3, which have been found to be chiral and electrically switchable photoferroelectric perovskite semiconductors. PbI6 octahedra determine the band structure and transport property, while the organic groups are responsible for chirality and ferroelectricity by removing the material's mirror and inversion symmetry, respectively (Fig. 1).

RESULTS AND DISCUSSION

We use a solution method to synthesize chiral perovskites from each molecular enantiomer, resulting in needle-like yellow crystals with millimeter dimensions (Fig. 2, A and B). Optical images (Fig. 2C) show that the materials from the R-CYHEA and S-CYHEA precursors exhibit similar shapes and colors (in unpolarized light). Nuclear magnetic resonance (NMR) and Fourier transform infrared spectroscopy

¹Department of Materials Science and Engineering, Rensselaer Polytechnic Institute, Troy, NY 12180, USA. ²Department of Physics, Rensselaer Polytechnic Institute, Troy, NY 12180, USA. ³Department of Chemistry, The Johns Hopkins University, Baltimore, MD 21218, USA. ⁴Faculty of Materials Science and Engineering, Kunming University of Science and Technology, Kunming, Yunnan 650093, China. ⁵X-ray Science Division, Advanced Photon Source, Argonne National Laboratory, Lemont, IL 60439, USA. ⁶Center for Materials, Devices, and Integrated Systems, Rensselaer Polytechnic Institute, Troy, NY 12180, USA.

^{*}These authors contributed equally to this work as first authors.

[†]Corresponding author. Email: wertze@rpi.edu (E.W.); sundar@rpi.edu (R.S.); shij4@rpi.edu (J.S.)

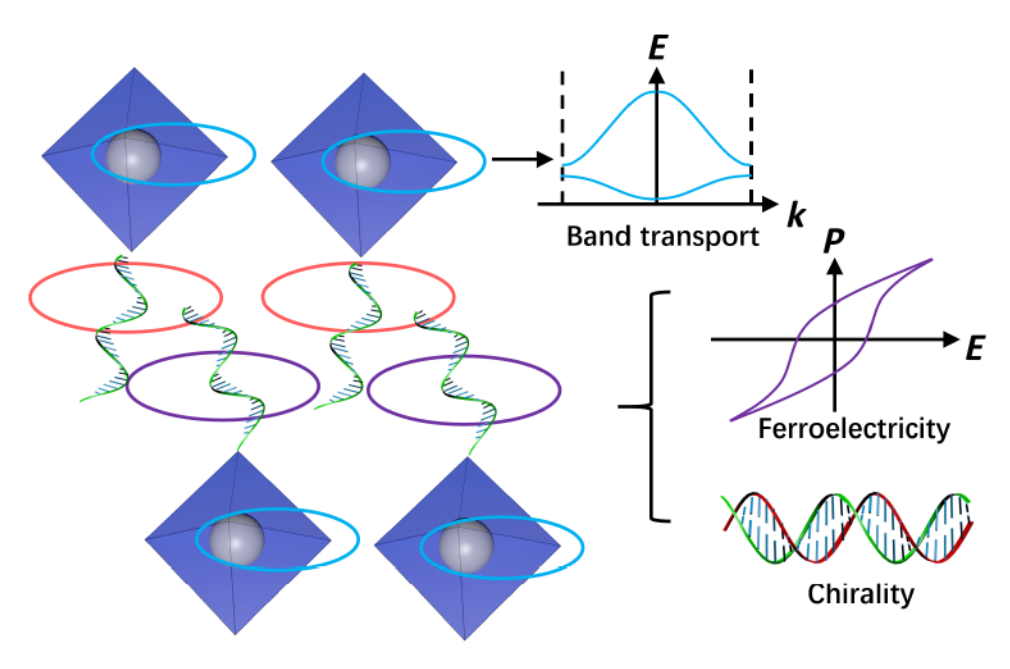


Fig. 1. Design principle. Lead halogen octahedra control the semiconducting property independently from the organic molecule that can be engineered to introduce a previously unknown properties, such as the simultaneous ferroelectricity and chirality achieved here.

(FTIR) confirm the identity of the organic molecule within each crystal, as shown in Fig. 2 (D and E). Most NMR peaks remain unchanged from the molecule, and a new peak at 7.6 parts per million (ppm) { 1 H NMR [500 MHz, dimethyl sulfoxide (DMSO)– d_{6}]: $\delta = 7.60$ (s, 3H), 3.00 to 2.98(m, 1H), 1.72 to 0.94 (m, 14H)} indicates the incomplete reaction of amino group and hydroiodic acid (HI) (fig. S1). The peaks in FTIR from N—H bonds at around 3200 cm⁻¹ are shifted from that in R-CYHEA/S-CYHEA because of the formation of —NH $_{3}$ + from —NH $_{2}$ (fig. S2). Simultaneously, Raman spectroscopy (see Materials and Methods) confirms the presence of lead iodine octahedra with the characteristic peak at around 100 cm⁻¹ seen for most lead iodide perovskites (25, 26), as shown in fig. S3 (see Materials and Methods for further details on the synthesis and spectroscopic measurements).

X-ray diffraction (XRD) then provides us with detailed structural information, as shown in figs. S4 to S8 and discussed further in Materials and Methods. Powder XRD of the materials synthesized from R-CYHEAI and S-CYHEAI are mutually quite similar to each other (figs. S4 and S5) and exhibit none of the peaks of PbI₂ or the molecular precursors. This indicates the structural similarity of the two enantiomers and complete transformation from the precursors. XRD of the films grown on different substrates are shown in figs. S6 to S8.

Rietveld refinements and single-crystal XRD measurements (Fig. 2, G and H) on the needle-like single crystals at -173° and 20°C (figs. S9 to S11 and tables S1 to S3) help determine lattice parameters and atomic positions in greater detail. The existence of a single fast axis in the transmission of linearly polarized white light (Fig. 2) and the Kikuchi pattern in our electron backscatter diffraction (EBSD) measurements (fig. S15) confirm that these needles are indeed single crystals. A combination of XRD crystal determination software, density measurements (fig. S16), and first-principles calculations (fig. S17) jointly establishes the space group of the crystal

to be $P2_1$ with angle $\beta = 89.5121^{\circ}$ (see more discussions on tables S1 to S3 and fig. S11). Figure 2G shows the single-crystal diffraction pattern of the crystal, and Fig. 2H presents the corresponding digitally reconstructed precession photograph. On the basis of first-principles calculations and single-crystal XRD at low and room temperatures, we find that the lattice expands slightly from a = 8.612 Å, b = 7.954 Å, and c = 21.719 Å at -173°C to a = 8.628 Å, b = 8.211 Å, and c = 22.994 Å at room temperature, with the angle and space group remaining unchanged. The structure and density identify the stoichiometry of the synthesized materials to be R-CYHEAPbI/S-CYHEAPbI₃ (Fig. 2I). First-principles density functional theory (DFT) calculations fill in the finer structural details beyond XRD resolution. These calculations show that opposite rotation of the amine groups on either side of the [001] plane breaks inversion symmetry along the b-direction, giving rise to polarization in the structure (fig. S17).

We then investigate the semiconducting property with optical and optoelectronic measurements. Photoluminescence spectroscopy (PL) measurements from a 405-nm excitation laser reveal a weak white PL (fig. S18), attributed to the Stokes process in low-dimensional halide perovskites (27–29), with response persisting to longer wavelengths including 635 nm as shown in figs. S21 and S22. A strong absorption transition ranging from ~360 to 410 nm indicates exitonic behavior (figs. S19 and S20) (30), once again consistent with the low-dimensional structure of the crystals (Fig. 2I).

Next, to test ferroelectricity in our material, we performed temperature-dependent second-harmonic generation (TD-SHG) to analyze this phase transition (Fig. 3A). The SHG signal markedly decreases (by half in intensity) at around 85°C, indicating a phase transition (at 100°C, the phase transition is complete) from a low-temperature SHG-active structure to a high-temperature structure, which shows no or much weaker SHG signal under our experiment condition. Figure S23 presents the SHG spectrum from the R

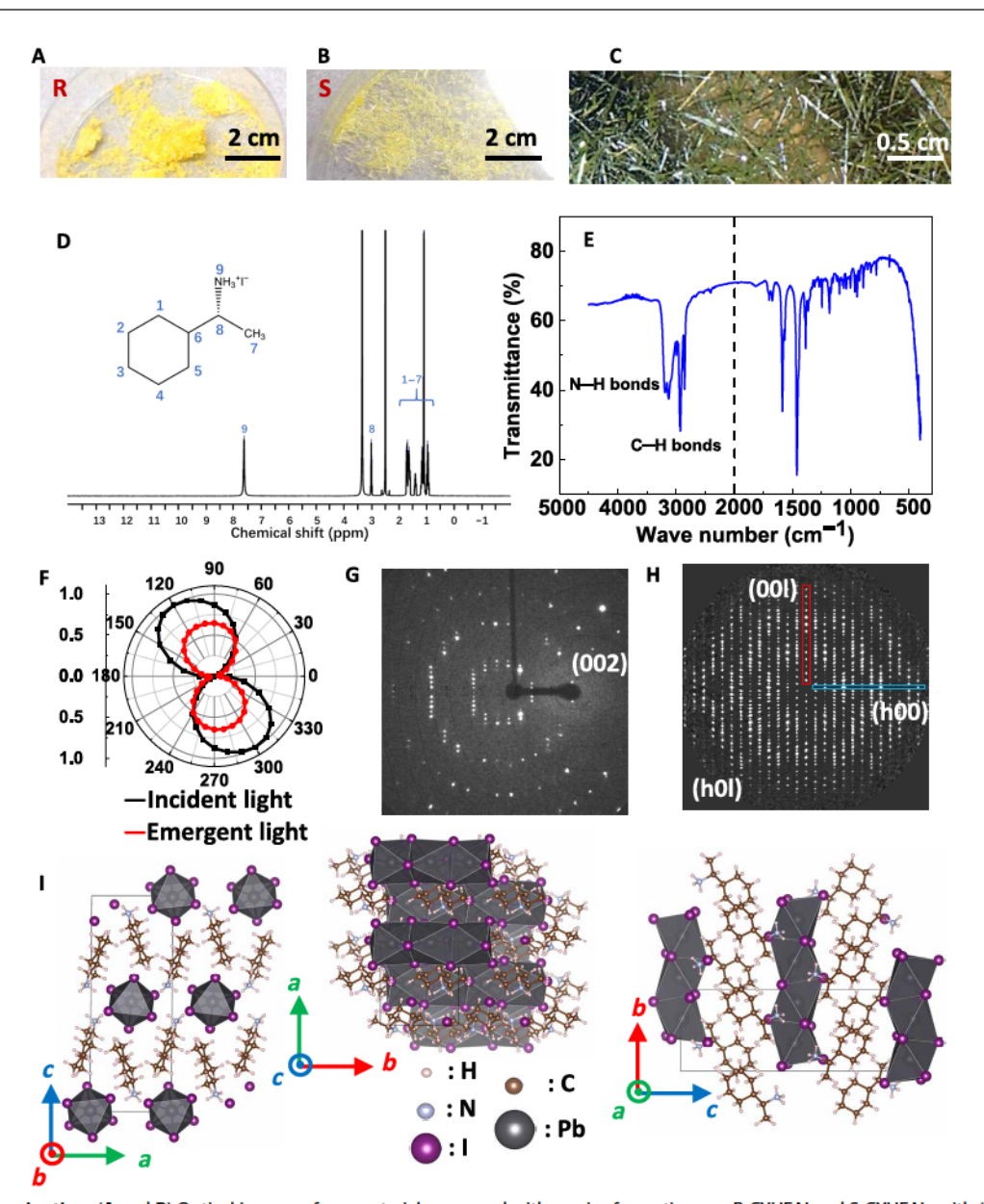


Fig. 2. Structure determination. (A and B) Optical images of our materials prepared with a pair of enantiomers, R-CYHEAI and S-CYHEAL, with (C) needle-like crystals. (Photo credit (A, B, and C): Yang Hu, Rensselaer Polytechnic Institute). (D) NMR results of our material (synthesized with R-CYHEA) dissolved in DMSO- d_6 . (E) FTIR result of our material (synthesized with S-CYHEA). N—H bond peaks shows up at around 3200 cm⁻¹, which is a little bit away from that of S-CYHEA but is almost the same as that of S-CYHEAI, indicating that this shift comes from the formation of —NH₃⁺. (F) Transmission spectrum with polarized light. The rotation of polarization direction indicates the existence of a single fast axis and the good single-crystal quality. (G) Single-crystal XRD diffraction pattern of our needle-like single crystal at -173° C. (H) Corresponding digitally reconstructed precession photograph of our crystal at 25° C, showing the (h0l) planes. (I) Schematic drawing of the structure of our 1D perovskite, where lead, iodine, carbon, nitrogen, and hydrogen atoms are represented by black, purple, brown, blue, and white spheres, respectively.

symmetry crystal. In addition, we used the double-wave technique (31–33) to characterize the polarization–electric field (PE) loops, as shown in Fig. 3B, clearly indicating the synthesized crystal to be ferroelectric (fig. S24). The polarization of around 0.03 μ C/cm² is small compared with commercial ferroelectric materials because of combination of a low intrinsic DFT-predicted polarization (see more discussion in fig. S17 and the associated description) and lack of alignment between the polarization and measurement axes (DFT predicts b axis, fig. S17). The orientation dependence of the polarization is further confirmed by direction-dependent PE loops in

fig. S26. Polarization endurance and retention results are shown in fig. S28. Further study shows that the polarization reaches $1.2\,\mu\text{C/cm}^2$ for a single-crystal sample, which will be discussed later.

Having established that our material is both ferroelectric and semiconducting, we measure the typical switchable diode effect (34–37) shown in Fig. 3C. The photoresponse of our devices was measured without external bias, and we found that the direction of photocurrent is dependent on the previous poling process (history of applied electric fields). Specifically, we find a negative photocurrent at 0 V after applying 10 V on the device for 200 s, and a positive photocurrent

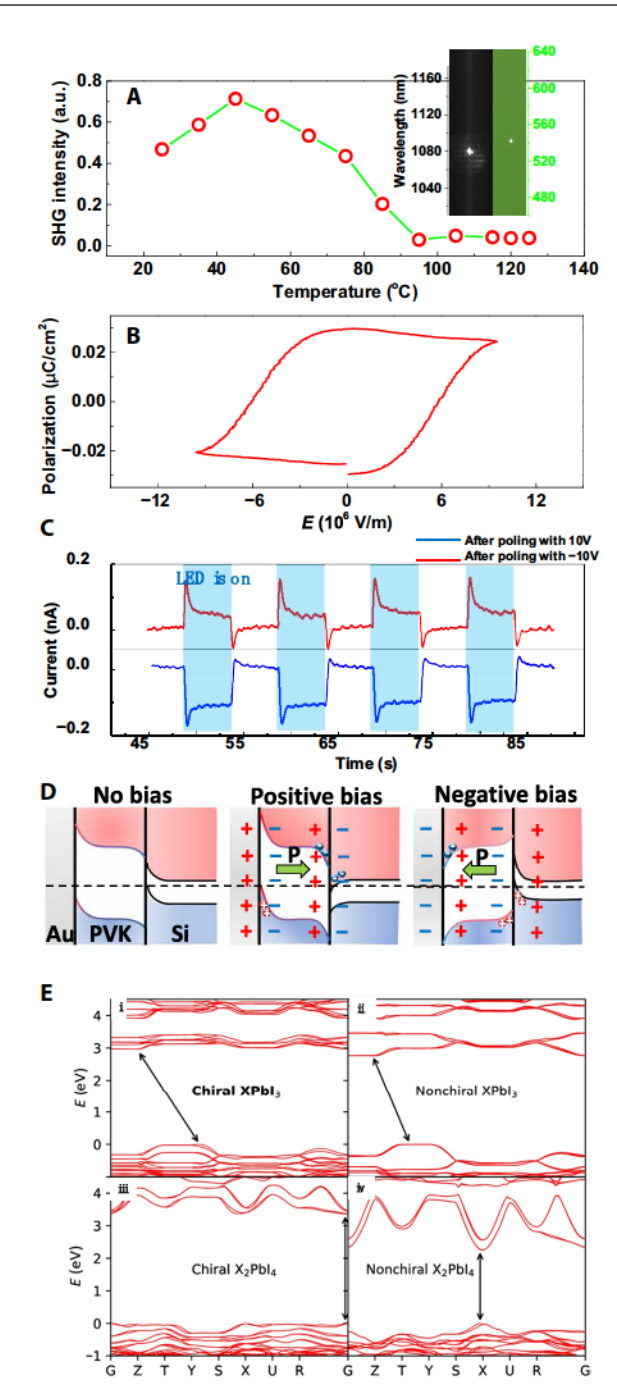


Fig. 3. Switchable photovoltaic ferroelectric effect. (A) TD-SHG reveals a transition from an inversion symmetry broken to an inversion-symmetric phase at 85°C. Inset: SHG peak at 540 nm from a 1080-nm infrared laser. a.u., arbitrary units. **(B)** PE loop of our perovskite confirming its ferroelectricity. Test was done at 800 Hz. **(C)** Switchable diode effect: After poling with $+10 \, \text{V}$ and $-10 \, \text{V}$ for 200 s, the photocurrent without bias is negative and positive, respectively, because of **(D)** band structure of our polycrystal device under zero bias, positive bias, and negative bias, respectively. A reversal in the band bending and resulting diode orientations are shown in the device. LED, light-emitting diode. PVK, perovskite. **(E)** Electronic band structure for chiral CYHEA (i and iii) and nonchiral CYHEA (ii and iv) XPbl₃ (i and ii) and X_2 Pbl₄ (iii and iv) stoichiometries including spin-orbit coupling (SOC). Bandgaps increase and switch from direct to indirect on going from X_2 Pbl₄ to XPbl₃ for each material. Including SOC brings the gap in much closer agreement with the experimental absorbance results as shown in fig. S20.

at 0 V if we applied –10 V instead. This arises from the switching of the ferroelectric, as shown in Fig. 3D. The polarization results in electric fields that result in opposite directions of band bending at each junction of the semiconductor with the contacts. Specifically, a positive (toward right) bias results in a diode with forward direction toward the right, leading to a negative photocurrent at zero bias. The negative bias reverses each of these directions. See figs. S29 and S30 for additional measurements and analysis on the absence of ion migration-induced switchable photoresponse (38). Both transport measurement–based ferroelectric PE loop and electrically field-switchable photovoltaic ferroelectricity demonstrated here, to our best knowledge, have not been revealed in other chiral perovskites yet (18).

To better understand the band structure of our material, we performed DFT calculations. Figure 3E shows the resulting HSE06 band structures for the stable chiral structure $XPbI_3$ determined using XRD in addition to an alternate X_2PbI_4 structure that is stable for other closely related halide perovskites, such as the nonchiral counterpart shown in Fig. 3E (ii and iv). The predicted bandgap with spin-orbit coupling included matches well with the experimental absorbance curves shown in fig. S20. Note that the bandgaps switch from direct in the X_2PbI_4 form to indirect in the $XPbI_3$ form for both the chiral and nonchiral materials. Analogous band structures calculated using the Perdew-Burke-Ernzerhof (39) are included in fig. S17.

Ferroelectric properties are further probed by a phase transition study on a single-crystal sample and device. Temperature-dependent synchrotron XRD on the single-crystal sample was performed to check the phase transition seen in our TD-SHG result. As shown in Fig. 4A, at around 100°C, the intensity of peak (021) markedly decreases, which indicates a phase transition. More detailed results are given in figs. S12 to S14 and movies S1 and S2. The space group after phase transition can only be determined to be P2₁2₁2₁ based on our XRD result (detailed analysis can be found in figs. S12 to S14) and pyroelectric study of single-crystal devices presented later. Hence, this phase transition is a ferroelectric to nonferroelectric one with a Curie temperature of around 100°C. A differential scanning calorimetry (DSC) test on the single-crystal sample was performed as another proof of phase transition. As shown in Fig. 4B, sudden increase and decrease in the DSC curves show up at around 100°C, indicating a phase transition. The temperature dependence of real part of dielectric constant on the single-crystal device is also performed (Fig. 4C). A peak shows up at around 100°C, which should also arise from phase transition.

Parasitic capacitance/current dominates under high voltages when our device does not follow a parallel capacitor configuration due to the 1D nature of our material. Hence, conventional PE loop measurement methods (such as Sawyer-Tower and double wave) would not be able to reveal the intrinsic property of such 1D material/device. Instead, we have conducted pyroelectric test to indirectly probe the ferroelectric properties (40). Switchable pyrocurrent was obtained (as shown in fig. S27), which is consistent with the properties of ferroelectric material. The temperature dependence of pyroelectric current was measured, as shown in Fig. 4D. This curve shows a peak at around 100°C, which indicates a phase transition, and fits well with theoretical calculation based on Landau theory (see fig. S27 for details). On the basis of this, higher temperature phase is nonferroelectric, as we saw no pyroelectric current after phase transition. The polarization at room temperature is around 1.2 μC/cm² obtained by

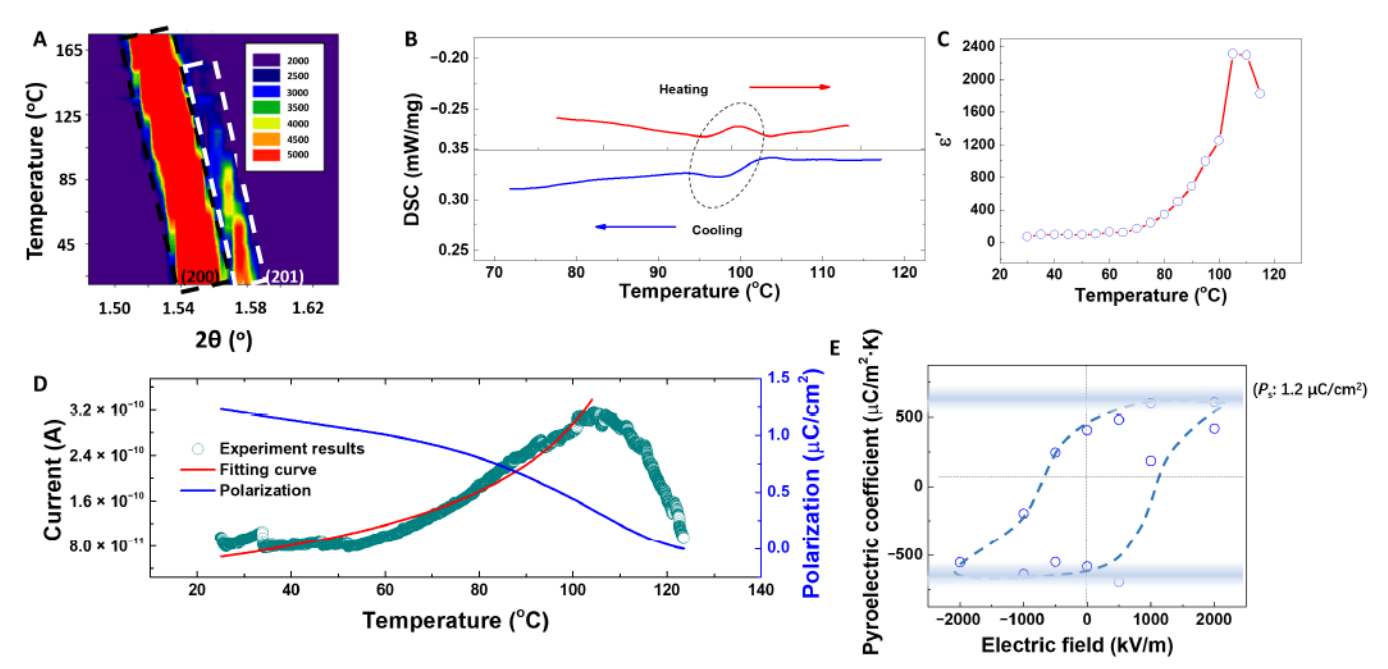


Fig. 4. Single-crystal phase transition and pyroelectric study. (A) Temperature-dependent synchrotron XRD results. Intensity of peak (201) markedly decreases, which indicates a phase transition at around 100°C. More detailed results can be found in the Supplementary Materials and movies S1 and S2. (B) DSC results. Sudden increase and decrease indicate a phase transition at around 100°C. (C) Temperature dependence of real part of dielectric constant. A peak at around 100°C indicates a phase transition. (D) Temperature dependence of pyroelectric current. The red and blue curves are fitting to Landau theory and polarization versus temperature curve obtained by integration, respectively. The peak at around 100°C indicates a phase transition. Our experiment results fit well with Landau theory, and the polarization at room temperature is around $1.2 \,\mu\text{C/cm}^2$ based on integration. (E) Pyroelectric coefficient versus poling electric field loop. Dash line is a trend line showing a hysteresis.

integration of pyroelectric current. As a substitution of PE loop, we also measured pyroelectric coefficient versus poling electric field (40). As shown in Fig. 4E, a hysteresis loop is observed, which indicates a ferroelectric performance.

Last, we use circular dichroism (CD) spectroscopy (see Materials and Methods) to confirm the chirality of the materials as shown in Fig. 5A. CD measures the difference in the absorption of left and right circularly polarized (LCP and RCP) lights, as shown in fig. S32 (18, 41–43). Figure 5B shows that R-CYHEAPbI₃ and S-CYHEAPbI₃ have opposite CD signals at same position, confirming them to be a pair of enantiomers. The maximum CD signal intensity (190 to 600 nm) of our perovskite far exceeds that of many common chiral materials, as shown in Fig. 5C. The intensity of CD signal can be described in the following equation (44, 45)

K is a constant to convert the unit of molecular extinction coefficient to molecular ellipticity.c, h, and N_A stand for light speed, reduced Planck constant, and Avogadro's number, respectively. β is a proportionality coefficient. Ψ_e and Ψ_g are the wave functions of ground state and excited state of electrons. μ and M represent the electric field dipole and magnetic field dipole moment operators, respectively. $\Delta \epsilon$ is CD signal. On the basis of this equation, CD signal becomes larger with larger electric field–dipole interaction, i.e., larger absorption coefficient. Hence, we may attribute our high CD signal to the higher absorption of our semiconducting material compared with traditional chiral organics (fig. S31).

CONCLUSION

In summary, we have theoretically predicted, experimentally synthesized, and comprehensively established a previously unknown low-dimensional hybrid perovskite material with both ferroelectricity and optical chirality. Structural, spectroscopy, and DFT analysis have shown that the pair of synthesized material enantiomers do not have inversion symmetry. Electrical and optoelectronic transport characterizations show the existence of PE loop, switchable and hysteresislike pyroelectric response, and a switchable photoferroelectric effect. On the basis of single-crystal material, temperature-dependent synchrotron XRD, DSC, temperature-dependent dielectric constant, and temperature-dependent pyroelectric current all show the existence of a ferroelectric-paraelectric phase transition at around 100°C. CD spectroscopy and theoretical analysis demonstrate the large chirality comparable to existing chiral organics. This new class of materials will form the foundation for exploiting chirality as an additional control on the ferroelectrically manipulated spin-orbit splitting in switchable Rashba-Dresselhaus materials (e.g., chirality-selected circular photogalvanic materials).

MATERIALS AND METHODS

Synthesis

R-CYHEAPbI₃/S-CYHEAPbI₃ was synthesized by a solution method. Lead iodine (PbI₂) (0.25 mmol; Sigma Aldrich), R-CYHEA/S-CYHEA (1 mmol; Sigma-Aldrich), and hydriodic acid aqueous solution (HI) (6 ml, ≥47.0%; Sigma-Aldrich) were mixed in a round-bottom flask in silicon oil bath. The flask was heated to 150°C for 2 hours with refluxing. Excess R-CYHEA/S-CYHEA and HI were used deliberately

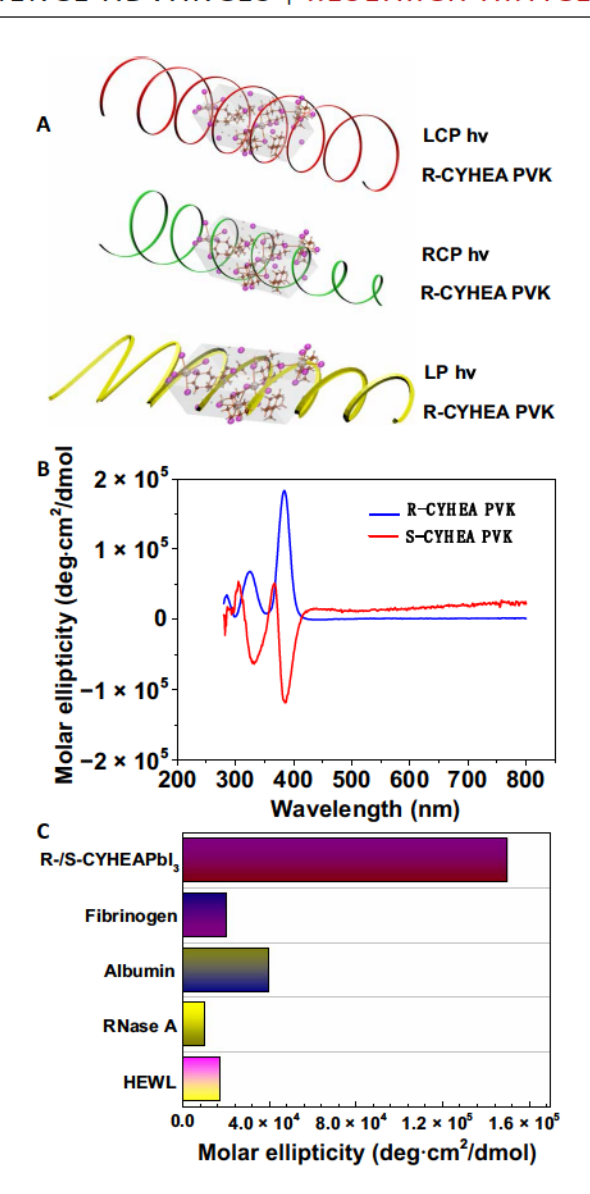


Fig. 5. Chirality. (A) Schematic of CD measurements: Chiral material absorbs different amount of LCP and RCP lights, changing linear polarization to elliptical. LP, linearly polarized. (B) CD spectrum of the synthesized crystals show opposite signals at the same position, indicating that they are enantiomers. (C) Our chiral ferroelectric material surpasses the CD signals of conventional chiral materials. RNase, ribonuclease; HEWL, hen egg white lysozyme.

to advance the reaction and to make sure that PbI_2 was completely consumed and can be removed after the reaction by filtration. After the heating process, a clear solution was obtained, and by slowly decreasing the temperature to room temperature at 0.1° C/min, large needle-like single crystals were successfully synthesized.

A chemical vapor deposition (CVD) method was also used to synthesize this material. We used a home-made CVD system (Extech 48VFL13 PID controller). Mica (SPI Grade V-5) was used as a substrate. The temperature at the furnace center was around 400°C, where one of the precursors, PbI₂, was placed. The other precursor, R-CYHEAI/S-CYHEAI, which was prepared by mixing R-CYHEA/S-CYHEA and HI in an ice water bath, was placed in an upstream position, 5 cm away from the zone center, while substrates was placed at downstream position. The system was pumped

to 0.5 torr before the deposition, after which the base pressure was maintained to be around 200 torr with a flow rate of 200 standard cubic centimeter per minute of argon. After 30-min growth, we successfully got some needle-like crystals on the substrate.

Thin film preparation

Thin films were prepared by a spin-coating method (Headway Manual Spin Coater). R-CYHEAPbI₃/S-CYHEAPbI₃ was dissolved in acetone, and the saturated solution was spin-coated on silicon wafers (Si, n-type,1.0 to 1.3 × 10¹⁵, 1/cm³-phosphor doped, Silicon Valley Microelectronics), fluorine-doped tin oxide-coated glasses (FTO; ~7 ohms/sq.; Sigma-Aldrich), freshly cleaved sodium chloride substrates (NaCl; Ted Pella Inc.), freshly cleaved potassium chloride substrates (KCl; Ted Pella Inc.), quartz slides (Technical Glass Products, Inc.) and glass slides (VWR) at 2000, 4000, 6000, 8000, and 10000 rpm for 30 s. After the spin-coating process, high-quality films were easily prepared, and annealing was not required.

Device preparation

For electrical measurements, 40-nm-thick round gold electrodes with a diameter of around 1 mm was deposited on the thin films by an electronic-beam (e-beam) deposition method to form usable devices with Temescal e-beam evaporator. Those devices were used for PE loop and photoresponse tests.

Our single-crystal device was prepared with a submillimeter-size single-crystal sample between two piles of silver paste on a glass substrate, forming a lateral device. This device was used for temperature-dependent dielectric constant measurement and pyroelectric tests (fig. S25).

NMR and FTIR measurement

Our material was dissolved in DMSO- d_6 for NMR measurement with 500 MHz Agilent NMR Spectrometer. A thin film on NaCl was used for FTIR measurement with a PerkinElmer Spectrum One FTIR spectrometer.

Optical measurements

Optical images and transmission of linear-polarized white light were measured with our Nikon Ti-S optical microscope. Thin films on KCl were used for Raman spectrum measurement with a WITec alpha300 confocal Raman microscope and a 532-nm continuous wave (CW) laser. PL measurement was done at room temperature with a home-built PL system [Thorlabs 4 Megapixel Monochrome Scientific charge-coupled device (CCD) camera, Princeton Instruments SP-2358 spectrograph, Nikon Ti-S optical microscope, and PicoQuant 405-nm pulsed laser]. Transmission spectrum was measured using a thin film on NaCl with a USB4000-UV-VIS spectrometer. The photoresponse of this material was measured with a home-made system (Autolab PGSTAT302N potentiostat and Thorlabs Compact Laser Diode Module with Shutter, 405/635 nm, 4.0 mW). Devices on FTO was used in these measurements. SHG measurement was performed with a home-made system (Keopsys KPS-BT2-YFL-1083-40-COL 1083 nm, 3-W CW fiber laser, Thorlabs 4 Megapixel Monochrome Scientific CCD camera, Princeton Instruments SP-2358 spectrograph, and Nikon Ti-S optical microscope). TD-SHG was performed with a Linkam Scientific Instruments TMS94 temperature controller.

XRD measurements

Powder XRD was performed using Cu Kα radiation on a Bruker D8 Focus diffractometer with a LynxEye detector. Rietveld refinements

were performed in TOPAS (Bruker AXS). Single-crystal XRD experiments were carried out by mounting needle-like crystals on a loop with a tiny amount of Paratone-N oil $[T = -163 (2)^{\circ}C]$ or epoxy (T = 25°C). All reflection intensities were measured using a SuperNova diffractometer (equipped with an Atlas detector) with Mo K α radiation ($\lambda = 0.71073$ Å) under the CrysAlisPro software suite (version 1.171.36.28, Agilent Technologies, 2012). CrysAlisPro was also used to index the cell dimensions and to perform data reduction. The generation of the initial models and subsequent structure refinements were conducted using SIR971 (46) and SHELXL-20132 (47), respectively. After the refinement of all of the atomic positions, the collected data were corrected for absorption (i.e., a face-indexed analytical absorption correction was applied using CrysAlisPro). The displacement parameters were then refined as anisotropic, and weighting schemes were applied during the final stages of refinement.

The crystallographic phase transition of 1D pervoskite single crystal was characterized by in situ temperature-dependent synchrotron high-energy XRD measurements, which were performed at the 11-ID-C beamline of the Advanced Photon Source at Argonne National Laboratory. High-energy x-rays of 0.11165-Å wavelength were used to obtain 2D diffraction patterns in the transmission geometry using a PerkinElmer large area detector placed downstream at 1.5 m away from the sample. The single-crystal Laue diffraction was collected as a function of heating temperature from 0° to 175°C in 5°C for each step. For each temperature point, the single longacquisition 2D image is the cumulative collection of the single-crystal diffraction as a function of rotation along the crystallographic zone axis of the longer side of the small needle-like single crystal. The temperature control was realized by an Oxford Instrument cryosteamer/heater system, which flushes the dry-heated N2 gas to the capillary glass tube enclosing the 1D perovskite needle-like small single crystal.

EBSD measurements

EBSD measurements were performed with an Oxford AZTEC system on our needle-like single crystals.

Electrical property measurements

PE loop measurements were performed with a home-built doublewave method system (BK Precision 2190D oscilloscope, AFG1062 Tektronix Arbitrary Waveform Generator) at different frequency. Detailed information about the double-wave method can be found in fig. S24.

Switchable diode effect was measured with a home-built system consisting of an Autolab PGSTAT302N potentiostat and a radio shack 10-mm blue light-emitting diode lamp (465 to 467.5 nm).

The temperature dependence of dielectric constant was measured with a home-built system (AFG1062 Tektronix Arbitrary Waveform Generator, BK Precision 2190D oscilloscope, and Falco Systems WMA-02 amplifier), and temperature was controlled by a cryostage (Linkam Scientific Instruments, TMS94). Impedance was measured, and dielectric constant was calculated

$$\varepsilon' = \frac{d}{2\pi f S \varepsilon_0} \frac{Z''}{Z'^2 + Z''^2} \tag{2}$$

 ε' is the real part of dielectric constant ($\varepsilon = \varepsilon' - i\varepsilon''$), d is the distance between two electrodes, S is the device area, f is the frequency of applied sine wave, ε_0 is the vacuum permittivity, and Z is the impedance (Z = Z' + Z'').

Pyroelectric current was measured with a potentiostat (Autolab PGSTAT302N) and a cryostage (Linkam Scientific Instruments, TMS94). Similar to PE loop measurements, pyroelectric coefficient versus poling electric field loop was obtained by poling our device at a series of voltage (2000, 1000, 500, 0, -500, -1000, -2000, -1000, -500, 0, 500, 1000, and 2000 V) and measured the pyroelectric coefficient after each poling. The temperature dependence of pyroelectric current was measured with a ramp speed of 10°C/min.

DSC measurements

DSC was measured with a differential scanning calorimeter (TA Instruments, DSC-Q100) under nitrogen atmosphere. Temperature range was set to be 20° to 120°C with a ramp speed of 10°C/min.

CD measurements

CD was performed on a Jasco 815 CD spectrometer.

DFT calculations

We performed DFT calculations using the open-source plane-wave software: JDFTx (48) with the Heyd-Scuseria-Ernzerhof (HSE06) (49) exchange-correlation functional, ultrasoft pseudopotentials (50), and a kinetic energy cutoff of 20 Hartrees for wave functions and 100 Hartrees for the charge density. We used DFT + D2 (51) pair-potential corrections for the van der Waals interaction and integrated over the Brillouin zone using a $2 \times 2 \times 1$ Γ -centered k-point mesh. The band structure was then calculated on a high-symmetry k-point path using maximally localized wannier functions.

SUPPLEMENTARY MATERIALS

Supplementary material for this article is available at http://advances.sciencemag.org/cgi/ content/full/6/9/eaay4213/DC1

Section S1. Structural characterization

Section S2. Optical characterization

Section S3. Ferroelectricity and pyroelectricity

Section S4. Photoferroelectricity

Section S5. Chirality

Fig. S1. NMR result of R-CYHEA.

Fig. S2. FTIR result of R-CYHEAI.

Fig. S3. Raman results of R-CYHEAPbl₃ on KCI.

Fig. S4. Powder XRD result of R-CYHEAPbl₃.

Fig. S5. Powder XRD result of S-CYHEAPbl₃. Fig. S6. XRD result of R-CYHEAPbl3 grown on Si.

Fig. S7. XRD result of R-CYHEAPbl₃ grown on mica.

Fig. S8. XRD result of R-CYHEAPbl₃ grown on NaCl.

Fig. S9. Rietveld modeling (red curve) of room temperature powder x-ray data (black crosses) and corresponding difference curve (blue) for powdered R-CYEHAPbl₃.

Fig. S10. Single-crystal XRD results of R-CYEHAPbl₃.

Fig. S11. Diffraction analysis.

Fig. S12. Single-crystal synchrotron XRD results.

Fig. S13. Analysis of synchtrotron diffraction result.

Fig. S14. Peak intensities have changed after temperature increases from 0° to 175°C.

Fig. S15. EBSD of single-crystal sample.

Fig. S16. Schematic drawing of the system that we used to measure the volume of the crystal in density determination.

Fig. S17. Theoretical electronic band structure and polarization.

Fig. S18. PL of R-CYEHAPbl₃.

Fig. S19. Transmission spectrum of S-CYEHAPbl₃.

Fig. S20. Absorption spectrum of S-CYEHAPbl₃

Fig. S21. Photoresponse of R-CYEHAPbl₃ on FTO under 405-nm laser.

Fig. S22. Photoresponse of R-CYEHAPbl₃ on FTO under 635-nm laser.

Fig. S23. SHG spectrum of R-CYEHAPbl₃.

Fig. S24. Comparison of Sawyer-Tower method and double wave method used in PE loop measurements.

Fig. S25. Our single-crystal device.

SCIENCE ADVANCES | RESEARCH ARTICLE

- Fig. S26. Orientation dependent of I-V curves of R-CYEHAPbl₃.
- Fig. S27. Pyroelectric results.
- Fig. S28. Polarization retention and fatigue endurance.
- Fig. S29. Photoferroelectric measurements.
- Fig. S30. Voltage-dependent photoresponse.
- Fig. S31. Comparison of the CD signals of chiral perovskites and chiral precursors.
- Fig. S32. Schematic drawing of the generation of ellipticity from different absorption to LCP and RCP.
- Table S1. Crystallographic and refinement parameters for R-CYEHAPbl₃.
- Table S2. Fractional coordinates and isotropic displacement parameters.
- Table S3. Bond lengths and angles.
- Movie S1. Laue diffraction patterns versus temperature.
- Movie S2. Zoom-in of Laue diffraction patterns versus temperature.

REFERENCES AND NOTES

- K. Yamauchi, P. Barone, T. Shishidou, T. Oguchi, S. Picozzi, Coupling ferroelectricity with spin-valley physics in oxide-based heterostructures. *Phys. Rev. Lett.* 115, 037602 (2015).
- D. Di Sante, P. Barone, R. Bertacco, S. Picozzi, Electric control of the giant Rashba effect in bulk GeTe. Adv. Mater. 25, 509–513 (2013).
- S. Picozzi, Ferroelectric Rashba semiconductors as a novel class of multifunctional materials. Front. Phys. 2, 10 (2014).
- D. Di Sante, P. Barone, A. Stroppa, K. F. Garrity, D. Vanderbilt, S. Picozzi, Intertwined Rashba, Dirac, and Weyl Fermions in hexagonal hyperferroelectrics. *Phys. Rev. Lett.* 117, 076401 (2016).
- J. He, D. Di Sante, R. Li, X.-Q. Chen, J. M. Rondinelli, C. Franchini, Tunable metal-insulator transition, Rashba effect and Weyl Fermions in a relativistic charge-ordered ferroelectric oxide. Nat. Commun. 9. 492 (2018).
- M. Kim, J. Im, A. J. Freeman, J. Ihm, H. Jin, Switchable S = 1/2 and J = 1/2 Rashba bands in ferroelectric halide perovskites. Proc. Natl. Acad. Sci. U.S.A. 111, 6900–6904 (2014).
- F. de Juan, A. G. Grushin, T. Morimoto, J. E. Moore, Quantized circular photogalvanic effect in Weyl semimetals. Nat. Commun. 8, 15995 (2017).
- P. Hosur, Circular photogalvanic effect on topological insulator surfaces: Berry-curvaturedependent response. Phys. Rev. B 83, 035309 (2011).
- K. Werner, Experimental and phenomenological aspects of circular birefringence and related properties in transparent crystals. Rep. Prog. Phys. 63, 1575 (2000).
- S. Yang, Z. Liu, S. Hu, A.-Z. Jin, H. Yang, S. Zhang, J. Li, C. Gu, Spin-selective transmission in chiral folded metasurfaces. *Nano Lett.* 19, 3432–3439 (2019).
- R. Ogier, Y. Fang, M. Käll, M. Svedendahl, Near-complete photon spin selectivity in a metasurface of anisotropic plasmonic antennas. *Phys. Rev. X* 5, 041019 (2015).
- R. Naaman, D. H. Waldeck, Spintronics and chirality: Spin selectivity in electron transport through chiral molecules. Annu. Rev. Phys. Chem. 66, 263–281 (2015).
- M. Kettner, B. Göhler, H. Zacharias, D. Mishra, V. Kiran, R. Naaman, C. Fontanesi,
 D. H. Waldeck, S. Sęk, J. Pawlowski, J. Juhaniewicz, Spin filtering in electron transport through chiral oligopeptides. J. Phys. Chem. C 119, 14542–14547 (2015).
- P. Qin, S. Tanaka, S. Ito, N. Tetreault, K. Manabe, H. Nishino, M. K. Nazeeruddin, M. Grätzel, Inorganic hole conductor-based lead halide perovskite solar cells with 12.4% conversion efficiency. *Nat. Commun.* 5, 3834 (2014).
- F. Hao, C. C. Stoumpos, D. H. Cao, R. P. H. Chang, M. G. Kanatzidis, Lead-free solid-state organic-inorganic halide perovskite solar cells. Nat. Photonics 8, 489–494 (2014).
- Y. Wang, X. Sun, R. Shivanna, Y. Yang, Z. Chen, Y. Guo, G.-C. Wang, E. Wertz, F. Deschler, Z. Cai, H. Zhou, T.-M. Lu, J. Shi, Photon transport in one-dimensional incommensurately epitaxial CsPbX₃ arrays. Nano Lett. 16, 7974–7981 (2016).
- Z. Chen, Y. Guo, E. Wertz, J. Shi, Merits and challenges of Ruddlesden–Popper soft halide perovskites in electro-optics and optoelectronics. Adv. Mater. 31, e1803514 (2019).
- C. K. Yang, W.-N. Chen, Y.-T. Ding, J. Wang, Y. Rao, W.-Q. Liao, Y.-Y. Tang, P.-F. Li, Z.-X. Wang, R.-G. Xiong, The first 2D homochiral lead iodide perovskite ferroelectrics: [R- and S-1-(4-Chlorophenyl)ethylammonium]₂Pbl₄. Adv. Mater. 31, e1808088 (2019).
- W.-Q. Liao, D. Zhao, Y.-Y. Tang, Y. Zhang, P.-F. Li, P.-P. Shi, X.-G. Chen, Y.-M. You, R.-G. Xiong, A molecular perovskite solid solution with piezoelectricity stronger than lead zirconate titanate. Science 363, 1206–1210 (2019).
- Y.-M. You, W.-Q. Liao, D. Zhao, H.-Y. Ye, Y. Zhang, Q. Zhou, X. Niu, J. Wang, P.-F. Li, D.-W. Fu, Z. Wang, S. Gao, K. Yang, J.-M. Liu, J. Li, Y. Yan, R.-G. Xiong, An organic-inorganic perovskite ferroelectric with large piezoelectric response. *Science* 357, 306–309 (2017).
- T.-T. Sha, Y.-A. Xiong, Q. Pan, X.-G. Chen, X.-J. Song, J. Yao, S.-R. Miao, Z.-Y. Jing, Z.-J. Feng, Y.-M. You, R.-G. Xiong, Fluorinated 2D lead iodide perovskite ferroelectrics. *Adv. Mater.* 31, e1901843 (2019).

- X.-N. Hua, W.-Q. Liao, Y.-Y. Tang, P.-F. Li, P.-P. Shi, D. Zhao, R.-G. Xiong, A room-temperature hybrid lead iodide perovskite ferroelectric. J. Am. Chem. Soc. 140, 12296–12302 (2018).
- H.-Y. Ye, W.-Q. Liao, C.-L. Hu, Y. Zhang, Y.-M. You, J.-G. Mao, P.-F. Li, R.-G. Xiong, Bandgap engineering of lead-halide perovskite-type ferroelectrics. Adv. Mater. 28, 2579–2586 (2016).
- W.-Q. Liao, Y. Zhang, C.-L. Hu, J.-G. Mao, H.-Y. Ye, P.-F. Li, S. D. Huang, R.-G. Xiong, A lead-halide perovskite molecular ferroelectric semiconductor. *Nat. Commun.* 6, 7338 (2015)
- W. Zhou, F. Sui, G. Zhong, G. Cheng, M. Pan, C. Yang, S. Ruan, Lattice dynamics and thermal stability of cubic-phase CsPbl₃ quantum dots. J. Phys. Chem. Lett. 9, 4915–4920 (2018).
- P. Pistor, A. Ruiz, A. Cabot, V. Izquierdo-Roca, Advanced Raman spectroscopy of methylammonium lead iodide: Development of a non-destructive characterisation methodology. Sci. Rep. 6, 35973 (2016).
- S.-T. Ha, C. Shen, J. Zhang, Q. Xiong, Laser cooling of organic-inorganic lead halide perovskites. Nat. Photonics 10, 115–121 (2016).
- J. Zhang, D. Li, R. Chen, Q. Xiong, Laser cooling of a semiconductor by 40 kelvin. Nature 493, 504–508 (2013).
- S. Li, J. Luo, J. Liu, J. Tang, Self-trapped excitons in all-inorganic halide perovskites: Fundamentals, status, and potential applications. J. Phys. Chem. Lett. 10, 1999–2007 (2019).
- W. J. Turner, W. E. Reese, G. D. Pettit, Exciton Absorption and Emission in InP. Phys. Rev. 136. A1467–A1470 (1964).
- M. Fukunaga, Y. Noda, Improvement of the double-wave method for ferroelectric hysteresis loops and its application to multiferroic euMn2O5. J. Korean Phys. Soc. 55, 888–892 (2009).
- M. Fukunaga, Y. Noda, New technique for measuring ferroelectric and antiferroelectric hysteresis loops. J. Phys. Soc. Jpn. 77, 064706 (2008).
- L. Hu, S. Dalgleish, M. M. Matsushita, H. Yoshikawa, K. Awaga, Storage of an electric field for photocurrent generation in ferroelectric-functionalized organic devices. *Nat. Commun.* 5, 3279 (2014).
- S. Hong, T. Choi, J. H. Jeon, Y. Kim, H. Lee, H.-Y. Joo, I. Hwang, J.-S. Kim, S.-O. Kang, S. V. Kalinin, B. H. Park, Large resistive switching in ferroelectric BiFeO₃ nano-island based switchable diodes. *Adv. Mater.* 25, 2339–2343 (2013).
- R. Guo, L. You, Y. Zhou, Z. S. Lim, X. Zou, L. Chen, R. Ramesh, J. Wang, Non-volatile memory based on the ferroelectric photovoltaic effect. *Nat. Commun.* 4, 1990 (2013).
- C. Ge, K.-J. Jin, C. Wang, H.-B. Lu, C. Wang, G.-Z. Yang, Numerical investigation into the switchable diode effect in metal-ferroelectric-metal structures. *Appl. Phys. Lett.* 99, 063509 (2011).
- C. Wang, K.-j. Jin, Z.-t. Xu, L. Wang, C. Ge, H.-b. Lu, H.-z. Guo, M. He, G.-z. Yang, Switchable diode effect and ferroelectric resistive switching in epitaxial BiFeO₃ thin films. Appl. Phys. Lett. 98, 192901 (2011).
- Z. Chen, Y. Wang, Y. Shi, B. Hsu, Z. Yang, J. Shi, Regulating carrier dynamics in single crystal halide perovskite via interface engineering and optical doping. Adv. Electron. Mater. 2, 1600248 (2016).
- J. P. Perdew, K. Burke, M. Ernzerhof, Generalized gradient approximation made simple. Phys. Rev. Lett. 77, 3865–3868 (1996).
- A. S. Sigov, M. I. Maleto, E. P. Pevtsov, V. V. Chernokozhin, Polarization, pyroelectric coefficient, and current-voltage characteristics of PZT thin films. *Ferroelectrics* 226, 183–190 (1999).
- H.-Y. Ye, Y.-Y. Tang, P.-F. Li, W.-Q. Liao, J.-X. Gao, X.-N. Hua, H. Cai, P.-P. Shi, Y.-M. You, R.-G. Xiong, Metal-free three-dimensional perovskite ferroelectrics. *Science* 361, 151–155 (2018).
- G. Long, C. Jiang, R. Sabatini, Z. Yang, M. Wei, L. N. Quan, Q. Liang, A. Rasmita, M. Askerka, G. Walters, X. Gong, J. Xing, X. Wen, R. Quintero-Bermudez, H. Yuan, G. Xing, X. R. Wang, D. Song, O. Voznyy, M. Zhang, S. Hoogland, W. Gao, Q. Xiong, E. H. Sargent, Spin control in reduced-dimensional chiral perovskites. *Nat. Photonics* 12, 528–533 (2018).
- J. Ahn, E. Lee, J. Tan, W. Yang, B. Kima, J. Moon, A new class of chiral semiconductors: Chiral-organic-molecule-incorporating organic-inorganic hybrid perovskites. *Mater. Horiz.* 4, 851–856 (2017).
- 44. J. A. Schellman, Symmetry rules for optical rotation. Acc. Chem. Res. 1, 144-151 (1968).
- J. A. Schellman, Circular dichroism and optical rotation. Chem. Rev. 75, 323–331 (1975)
- A. Altomare, M. C. Burla, M. Camalli, G. L. Cascarano, C. Giacovazzo, A. Guagliardi, A. G. G. Moliterni, G. Polidori, R. Spagna, SIR97: A new tool for crystal structure determination and refinement. *J. Appl. Cryst.* 32, 115–119 (1999).
- 47. G. Sheldrick, A short history of SHELX. Acta Crystallogr. A 64, 112-122 (2008).
- R. Sundararaman, K. Letchworth-Weaver, K. A. Schwarz, D. Gunceler, Y. Ozhabes, T. A. Arias, JDFTx: Software for joint density-functional theory. Softwarex 6, 278–284 (2017).

SCIENCE ADVANCES | RESEARCH ARTICLE

- J. Heyd, G. E. Scuseria, M. Ernzerhof, Hybrid functionals based on a screened Coulomb potential. J. Chem. Phys. 118, 8207

 –8215 (2003).
- K. F. Garrity, J. W. Bennett, K. M. Rabe, D. Vanderbilt, Pseudopotentials for high-throughput DFT calculations. Comp. Mater. Sci. 81, 446–452 (2014).
- S. Grimme, Semiempirical GGA-type density functional constructed with a long-range dispersion correction. J. Comput. Chem. 27, 1787–1799 (2006).

Acknowledgments

Funding: J.S. and R.S. acknowledge start-up funding from the Department of Materials Science and Engineering at Rensselaer Polytechnic Institute, NSF under award nos. 1635520, 1916652, and 1712752, the Air Force Office of Scientific Research under award no. FA9550-18-1-0116, and the Office of Naval Research under award no. N000141812408. L.Z. thanks the funding support from the New York State's Empire State Development's Division of Science, Technology and Innovation through Focus Center Contract C150117. Calculations were performed at the Center for Computational Innovations at Rensselaer Polytechnic Institute. This research used resources of the Advanced Photon Source, a U.S. Department of Energy (DOE) Office of Science User Facility operated for the DOE Office of Science by Argonne National Laboratory under contract no. DE-AC02-06CH11357. This material is partially based on work supported by the NSF-MIP Platform for the Accelerated Realization, Analysis, and Discovery of Interface Materials (PARADIM) under cooperative agreement no. DMR-1539918. Author contributions: Y.H. and Z.C. grew the materials and fabricated the films. Y.H., Z.C., and J.J. conducted the electrical and optoelectrical transport studies. F.F. and R.S. conducted

computational simulations. H.Z. and Y.R. conducted and analyzed temperature-dependent synchrotron XRD. W.A.P. and M.A.S. conducted and analyzed single-crystal XRD. Z.Z. and E.F.P. conducted and analyzed DSC and NMR results. Y.H., Y.G., R.H., J.J., L.Z., and Y.W. conducted device fabrication. Y.H. and Y.G. conducted and analyzed CD spectra. B.W. and D.G. conducted FTIR study and helped on XRD study. Y.H. and J.J. conducted and analyzed SHG. L.Z. conducted and analyzed atomic force microscopy and scanning electron microscopy studies. Z.L. and X.S. conducted EBSD study. X.S. conducted physical vapor deposition growth. Y.H. and F.F. wrote the manuscript. T.-M.L., E.W., R.S., J.F., and J.S. all participated in the analysis of data and revision of the manuscript. J.S. and R.S. conceived and supervised the project. Competing Interests: The authors declare that they have no competing interests. Data and materials availability: All data needed to evaluate the conclusions in the paper are present in the paper and/or the Supplementary Materials. Additional data related to this paper may be requested from the authors.

Submitted 17 June 2019 Accepted 5 December 2019 Published 28 February 2020 10.1126/sciadv.aay4213

Citation: Y. Hu, F. Florio, Z. Chen, W. A. Phelan, M. A. Siegler, Z. Zhou, Y. Guo, R. Hawks, J. Jiang, J. Feng, L. Zhang, B. Wang, Y. Wang, D. Gall, E. F. Palermo, Z. Lu, X. Sun, T.-M. Lu, H. Zhou, Y. Ren, E. Wertz, R. Sundararaman, J. Shi, A chiral switchable photovoltaic ferroelectric 1D perovskite. *Sci. Adv.* 6, eaay4213 (2020).



A chiral switchable photovoltaic ferroelectric 1D perovskite

Yang Hu, Fred Florio, Zhizhong Chen, W. Adam Phelan, Maxime A. Siegler, Zhe Zhou, Yuwei Guo, Ryan Hawks, Jie Jiang, Jing Feng, Lifu Zhang, Baiwei Wang, Yiping Wang, Daniel Gall, Edmund F. Palermo, Zonghuan Lu, Xin Sun, Toh-Ming Lu, Hua Zhou, Yang Ren, Esther Wertz, Ravishankar Sundararaman and Jian Shi

Sci Adv **6** (9), eaay4213. DOI: 10.1126/sciadv.aay4213

ARTICLE TOOLS http://advances.sciencemag.org/content/6/9/eaay4213

SUPPLEMENTARY http://advances.sciencemag.org/content/suppl/2020/02/24/6.9.eaay4213.DC1

REFERENCES This article cites 51 articles, 4 of which you can access for free

http://advances.sciencemag.org/content/6/9/eaay4213#BIBL

PERMISSIONS http://www.sciencemag.org/help/reprints-and-permissions

Use of this article is subject to the Terms of Service